Original Article

Bio-inspired ultrasonochemical synthesis of blooming flower like ZnO hierarchical architectures and their excellent biostatic performance

H.J. Amith Yadav [a], B. Eraiah [a, *], H. Nagabhushana [b, **], G.P. Darshan [c], B. Daruka Prasad [d], M.K. Sateesh [e], S.C. Sharma [f, g], P.Hema Prabha [h]

[a] Department of Physics, Bangalore University, Bangalore 560056, India
[b] Prof. C.N.R. Rao Center for Advanced Materials, Tumkur University, Tumkur 572103, India
[c] Department of Physics, Acharya Institute of Graduate Studies, Bangalore 560107, India
[d] Department of Physics, B M S Institute of Technology, VTU Affiliated, Bangalore 560064, India
[e] Molecular Diagnostics and Nanotechnology Laboratories, Department of Microbiology and Biotechnology, Bangalore University, Bangalore 560056, India
[f] Department of Mechanical Engineering, Jain University, Jain Group of Institutions, Bangalore 560069, India
[g] Avinashilingam Institute for Home Science and Higher Education for Women University, Coimbatore 641043, India
[h] Department of Food Processing and Preservation Technology, Avinashilingam Institute for Home Science and Higher Education for Women University, Coimbatore 641043, India

ABSTRACT

Novel three dimensional (3D) ZnO hierarchical architectures were fabricated by a bio-inspired ultrasound assisted sonochemical route using self-sacrificial Aloe Vera (A.V.) gel as a bio-surfactant. The emergence of 3D superstructures (SS) is of essential interest, and the ability to program their form has practical ramifications in fields such as optics, biological activity, and catalysis and creates a bouquet of assembled SS with unprecedented levels of complexity and precision. These results outline a nanotechnology strategy for "collaborating" with self-assembly processes in real time to build SS architecture. The structural analysis exhibits that the ZnO SS were high purity without any secondary phases. Photoluminescence (PL) studies indicate that the zinc vacancies (V_{2n}) and singly ionized oxygen vacancies (Vo^+) located on the surface of ZnO. Further, we report a 'smart' bio-static ZnO SS, which might prevent build-up of active antimicrobial material in the environment. Precisely localized control of activity is achieved, allowing the growth of bacteria to be confined to defined patterns, which has potential for the development of treatments that avoid interference with the endogenous microbial population in other parts of the organism.

© 2017 Publishing services by Elsevier B.V. on behalf of Vietnam National University, Hanoi. This is an open access article under the CC BY license (http://creativecommons.org/licenses/by/4.0/).

1. Introduction

Nowadays, self-assembly of nanoscale building blocks into complex structures has been a hot spot in the fabrication of nanostructured materials. Many researchers have paid considerable attention to complex micro/nano-structures, especially three-dimensional (3D) SS that are assembled by 1D and 2D nanoscale building blocks such as nanowires, nanorods, nanoplates and nanosheets [1–3]. Comparing mono-morphological structures, the building blocks which create SS are of micrometer and nanometer scale will exhibit outstanding optical, electronic, and catalytic properties [4]. Thus, SS have a wide range of potential applications, including solar cells, photocatalysts, gas sensors and etc. [5,6].

Current development in nanotechnology has engineered nanomaterials that are possibly safe toward human welfare [7,8]. The early phase of this technology, toxic chemicals and harsh reaction conditions are followed. To overcome these problems, non-toxic, bio-compatible and eco-friendly fabrication techniques via 'green' approach are essential [9,10]. Compared to most of the synthesis routes, ultrasound assisted sonochemical route has wide advantages, namely, decrease in reaction time, mild reaction conditions, versatility with solvents, prevention of toxic chemicals, high

calcination temperature, inexpensive, economical and etc. [11,12]. When ultrasound was irradiated in a liquid reaction mixture, it spreads through a series of rarefaction and compression waves. Cavitation bubbles are formed due to suppression of the attractive forces of the liquid molecules. Implosions of collapsing bubbles produce energy for mechanical and chemical effects [13,14].

ZnO has employed an inevitable role among all other metal oxides due to its rich variety of structures. Further, ZnO exhibits unique properties, namely, non-toxic, good electrical conductivity, good transparency, high electron mobility, wide band gap with high exciton binding energy, enhanced luminescence, low cost and etc. [15]. Additionally, ZnO can be effortlessly synthesized by following various routes, namely, thermal evaporation [16], chemical vapor deposition (CVD) [17], molecular beam epitaxial [18], magnetron sputtering [19], and pulsed laser deposition [20]. To date, ZnO Wurtzite can be tailored by various methods to achieve various SS such as nano belts, nano cage, nano rings, needle-like nano whiskers, nanotubes, nanowires, nanorods, nano beads, nano forest, spherical, bundles, and etc. [21,22]. All such morphologies possess a variety of useful applications which prompt a wide range of subsequent research on synthesis of ZnO. Still a remarkable challenge for the fabrication of ZnO flower-like SS via simple accurate synthesis route.

In this study, a facile, economical and eco-friendly ultrasound assisted sonochemical route has been introduced to fabricate various 3D ZnO SS. Morphological changes with various experimental parameters, namely, ultrasound irradiation time, concentration of surfactant, pH level of solution, and ultrasound frequency are systematically studied. Further, the biostatic performance of prepared ZnO samples was extensively studied.

2. Synthesis and characterization

The 3D ZnO SS were fabricated via ultrasound assisted sonochemical route using bio-template *A.V.* gel as a bio-surfactant. The precursor solution of Zinc nitrate [Zn (NO$_3$)$_3$] was prepared by dissolving in 50 mL of distilled water. 5 mL of *A.V.* gel extract was dissolved in 100 mL double distilled water and added to the resultant precursor solution slowly. The detailed procedure for the extraction of *A.V.* gel was determined elsewhere [10]. Then, the solution mixture of Zinc nitrate and *A.V.* gel extract was stirred ultrasonically (ultrasonic frequency ~ 20 kHz, power ~ 300 W) at a fixed temperature of ~60 °C and by varying sonication time (1−6 h). The pH of the solution was maintained by adding NaOH to resultant mixture. The experiment was repeated with varying *A.V.* gel concentration, pH values and sonication power at a fixed time. The solution was kept undisturbed until a white precipitate was formed. The precipitate was filtered and washed several times with distilled water and ethanol to remove any unreacted material in the centrifuge instrument. The precipitated powder was dried at ~60 °C for 3 h in a vacuum oven and used for further characterizations. The schematic representation for the synthesis of the 3D ZnO SS was shown in Fig. 1.

Phase purity and crystallinity of ZnO SS were recorded using a powder X-ray diffractometer (XRD, Shimadzu 7000), Cu-k$_\alpha$ (1.541 Å) radiation with nickel filter. The data were collected over a 2θ range from 20° to 80° at intervals of 0.017° with a counting time of 1 s per step. Morphological studies were performed on a Hitachi table top, Model TM 3000 and Hitachi H-8100 accelerating voltage up to 200 KV, LaB$_6$ filament equipped with EDS (Kevex sigma TM Quasar, USA). The Diffuse reflectance (DR) spectroscopy of the prepared samples was recorded on spectrometer PerkinElmer (Lambda-35) using the white BaSO$_4$ powder as a reference standard. Jobin Yvon Spectroflourimeter Fluorolog-3 was used to measure PL properties.
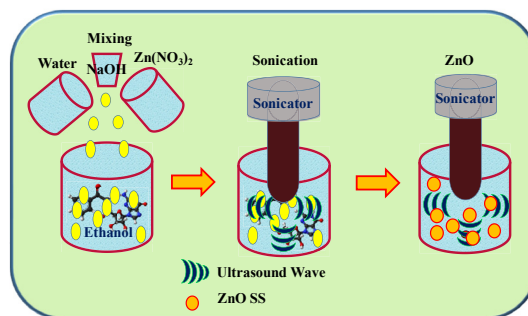

Fig. 1. Schematic representation for the synthesis of 3D ZnO SS by ultrasound assisted sonochemical route by using self-sacrificial *A.V.* gel extract as a surfactant.

2.1. Antibacterial assay of hierarchical ZnO structures

Antimicrobial activities of the 3D ZnO SS are tested using four common bacterial pathogens. Two strains of Gram-positive bacteria *Bacillus subtilis* (ATCC 6633) and *Staphylococcus aureus* (ATCC 6538) as well as two Gram-negative bacteria *Escherichia coli* (ATCC 8739) and *Pseudomonas aeruginosa* (ATCC 9027) were selected. The microorganisms were cultured on Mueller-Hinton agar (Hi-Media, Mumbai, India) at ~37 °C for ~24 h in aerobic conditions. Then, a suspension of bacterial strains with an optical density of McFarland of 0.5 (1×10^8 CFU/mL) was made in an isotonic Sodium Chloride (0.85%) solution. Afterward, this solution was diluted ten times (1×10^7 CFU/mL) and used immediately for testing as inoculum in the further experiments.

2.2. Determination of minimum inhibitory concentration (MIC) and minimum bactericidal concentration (MBC) of 3D ZnO SS

The antibacterial activity, MIC, and MBC of the ZnO SS were determined by the broth micro dilution method. MIC was determined according to Clinical and Laboratory Standards Institute (CLSI, 2006) with some adaptations using 96-well micro dilution plate where strains (concentration of 1×10^7 CFU/mL) were exposed to ten-fold dilution series of the ZnO SS ranging from 25 to 0.000025 μg/mL. The same procedure was used to determine the MIC of the positive (tetracycline), negative controls and ZnO SS. MIC was defined as the lowest concentration of agent that restricted growth to a level lower than 0.05 at 600 nm (no visible growth). The tetracycline (25 μg/mL) was used as standard antibiotic effective against the bacterial strains tested as the positive control. Sterile Mueller-Hinton broth with 0.85% NaCl was used as the negative control. The 20 μL of the bacterial suspension (10^7 CFU/mL) was added to each well and incubated at 37 °C for 24 h in bacteriological incubator. All the assays were performed in triplicate. Subsequently, the MIC values of the samples were detected by the addition of 25 μL of iodonitrotetrazolium chloride (INT at 0.5 mg/mL) in each well after 24 h incubation period. The micro titre plates were additionally incubated at 37 °C for 60 min. MICs of each sample were determined as the lowest concentration of the drug that stopped the color change from colorless to red. MBC determination was done by using 50 μL of cultured aliquots (without INT) was streaked onto the Mueller Hinton (MH) agar in petri plate and incubated for 24 h at 37 °C. The lowest concentration that indicated complete non-appearance of the bacterial growth on MH agar surface was considered as the MBC.

2.3. Antifungal assay of the synthesized 3D ZnO SS

The *Phomopsis azadirachtae* (neem die-back disease pathogen) and *Fusarium oxysporum* (tomato blight pathogen) were obtained

from the culture collection center of the Microbiology laboratory at the Bangalore University, Bangalore, Karnataka, India. *P. azadirachtae* and *F. oxysporum* were grown on SDA at 25 ± 1 °C and incubated with the alternative cycle of dark and light. Antifungal assay was accomplished by the agar dilution method or food poison method with slight modifications. The autoclaved SDA media adjusted such a way that the different concentrations of synthesized ZnO 3D architectures (100, 200, 300 and 400 μg/mL) and ZnO SS-free solution were

poured into the Petridishes (9 cm diameter). The fungal organisms were inoculated after the SDA media solidified. A mycelial agar disc pierced aseptically with a sterile cork borer of 5 mm diameter from the margin of 7-day-old fungal cultures were placed in the center of each Petri dish on different concentrations of ZnO SS and controls media. All the Petri dish with the inoculated mycelial agar disc was then incubated at 25 ± 1 °C for seven days. The effectiveness of ZnO SS on fungal growth was assessed at the time intervals of 7 days by
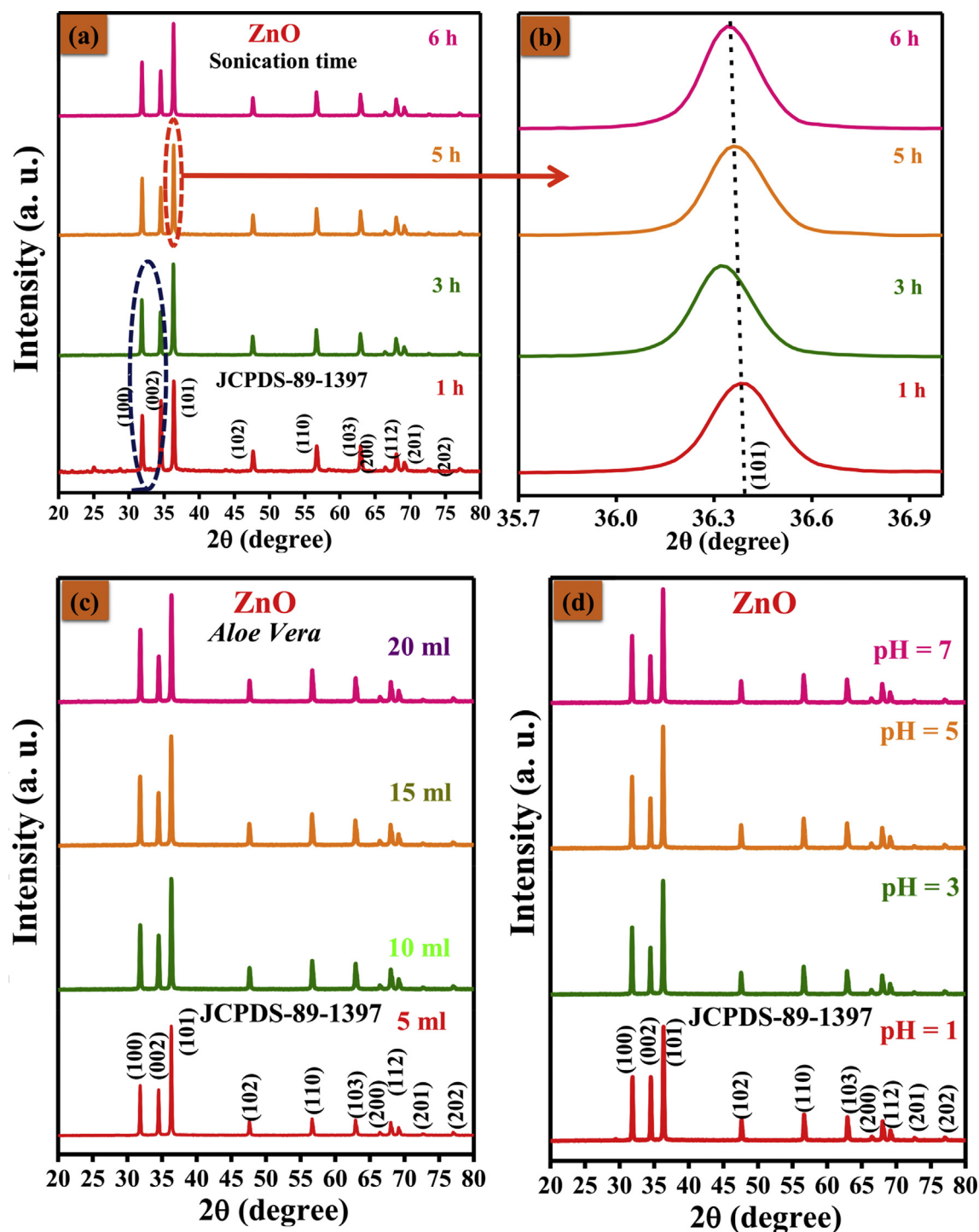

Fig. 2. PXRD patterns of ZnO SS synthesized with different (a) ultrasound irradiation times (1–6 h), (b) enlarged portion of peak 36.12°, (c) *A.V.* gel concentrations (5–20 mL) and (d) pH (1–7) values.

Table 1
Estimated average crystalline size and energy band gap values of ZnO SS fabricated at various reaction parameters.

Reaction parameters		Scherrer's approach	Energy gap (eV)
A.V. (mL) *concentration*	5	40	3.03
	10	36	3.05
	15	33	2.95
	20	30	2.97
Ultrasound irradiation time (h)	1	42	3.68
	2	42	3.06
	3	40	3.00
	4	34	3.08
pH value	1	38	3.10
	3	37	2.99
	5	36	2.97
	7	31	3.14

measuring the diameter of fungal colonies. All tests were performed in triplicate and the values were expressed in centimeters. The antifungal index of ZnO SS was determined as mentioned below:

$$\text{Percentage inhibition} = \frac{dc - dt}{dc} \times 100 \qquad (1)$$

where dc and dt; the average increase in mycelia growth in control and treatment respectively.

2.4. Statistical analysis

The antifungal experimental data were analyzed by mean ± SE subjected to multivariate analysis. Means are separated by Duncan's multiple range tests at 0.5 significant ($P < 0.05$) using SPSS software (version 20).

3. Results and discussion

Fig. 2(a, c and d) shows PXRD profiles of 3D ZnO architectures fabricated by varying experimental parameters, namely ultrasound irradiation time (1–6 h), *A.V.* gel concentration (5–20 mL) and pH values (1–7). The spectra exhibits single and sharp diffraction peaks which confirms the formation of single hexagonal Wurtzite phase and indexed according to the standard JCPDS (Card No. 36-1451) [23]. No impurity peaks were observed, indicating that the various experimental parameters do not influence the crystal structure. A small peak shift (101) ($2\theta = 36.28°-36.15°$) with increment of ultrasound irradiation time was observed in Fig. 2(b). This observation was due to change in stress induced by ultrasonic wave which deposits an enormous amount of energy into the electronic system of the atoms which may transfer to the crystal lattice by electron–phonon coupling [24]. Generally, the relative intensities of the diffraction peaks were implying that the preferred orientations
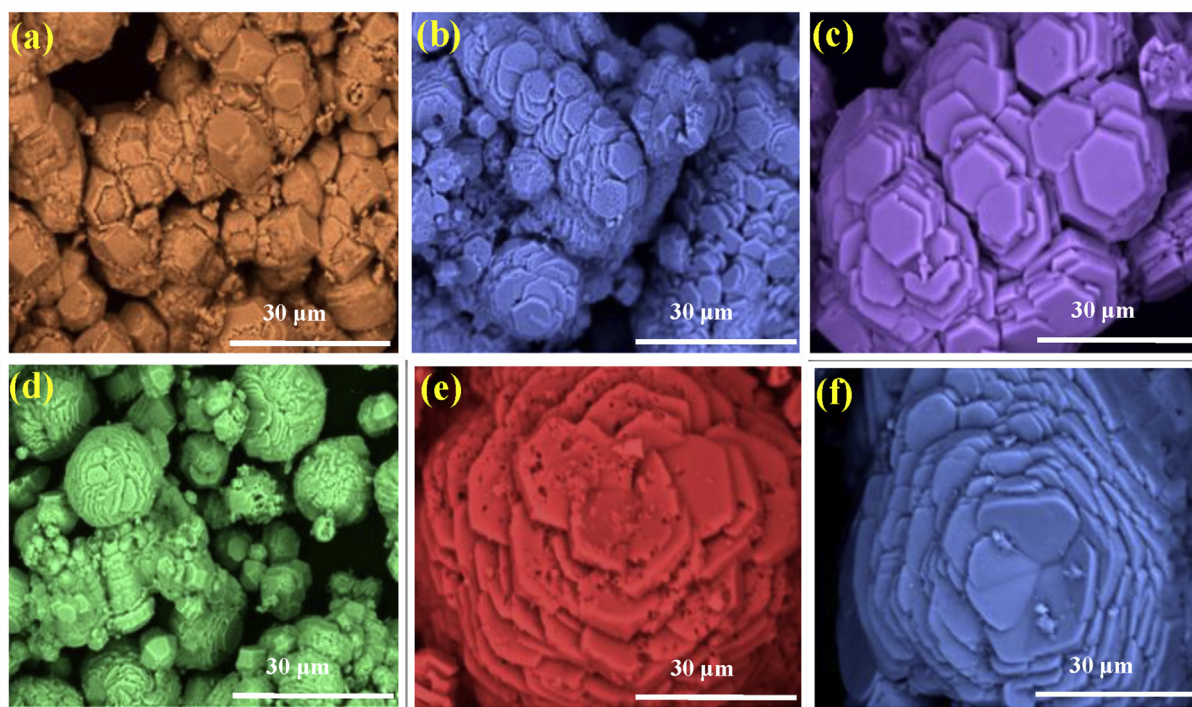

Fig. 3. Exotic hierarchical structures of ultrasonically fabricated 3D ZnO synthesized at different ultrasound irradiation time (1, 2, 3, 4, 5 and 6 h) while *A.V.* gel concentration and pH value were fixed to 35 mL and 11 respectively.
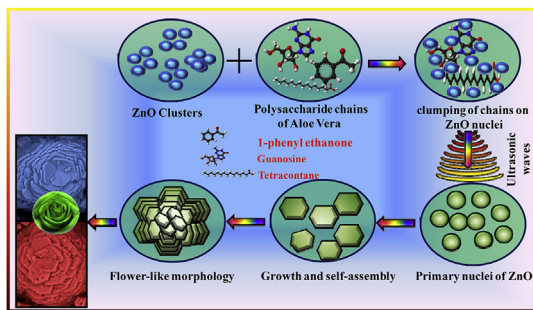
Fig. 4. Schematic representation of the formation of blooming flower-like ZnO architectures.

occurred during crystallization [25]. In fact, small and large values of the planes (100)/(002) ratio suggests the extensional and shortening of crystal growth along c-axis respectively. In the present investigation, the peak intensity ratio was found to be ~1.253, indicates the degree of anisotropy and shortening of crystal growth along c-axis of synthesized ZnO SS.

Average crystallite size (D) of the prepared ZnO SS was estimated by utilizing Scherrer's relation:

$$D = K\lambda/\beta \cos\theta \qquad (2)$$

where λ; wavelength of the X-rays (1.540 Å), K; shape factor (0.9), β; FWHM and θ; Bragg's angle. The values of 'D' were estimated and listed in Table 1.

Fig. 3 depicts SEM micrographs of the 3D ZnO SS fabricated with different sonication times (1, 2, 3, 4, 5 and 6 h) while *A.V.* gel

concentration and pH value were fixed to 35 mL and 11 respectively. From the images, it was evident that ultrasound irradiation time during synthesis significantly alters the morphological features. After 1 h ultrasound irradiation time, large numbers of hexagonal studs like structures were observed (Fig. 3(a)). When the ultrasound irradiation time was increased to 2 and 3 h, hexagonal studs like structures undergo Ostwald ripening to form hexagonal plates like structures were identified in Fig. 3(b and c). However, when the ultrasound irradiation time was extended to 4 and 5 h, formed hexagonal plates were undergoing self-assembly to form a flower-like hierarchical structure, but it was not well developed (Fig. 3(d and e)). Further, when ultrasound irradiation time was prolonged to 6 h, finely defined flower-like architecture was observed (Fig. 3(f)). The schematic representation of formation process of blooming flower-like ZnO architectures was shown in Fig. 4.

Exotic hierarchical structures of ultrasonically fabricated 3D ZnO at different pH value (5, 7, 9 and 11) synthesized with ultrasound irradiation time (6 h) and *A.V.* gel concentration (35 mL) was depicted in Fig. 5. It was apparent from SEM images that, the pH value of the solution may considerably influence the morphology of the ZnO product. When the precursor solution was maintained to pH = 5, growth staged randomly oriented hexagonal disks starts self-assembling side by side to form closed corral (Fig. 5(a)). In the growth stage, many of the small assembly units having reduced surface energy spread out divergently to form hierarchical SS. As the pH of the solution was prolonged, the randomly oriented disks start assembling in order direction to form condensed corral ZnO architectures (Fig. 5(b−f)). To achieve this kind hierarchical architectures, several factors may influence, namely crystal face attraction, electrostatic and dipolar fields associated with the aggregate, Vander Waals forces, intrinsic structures and external factors [26].
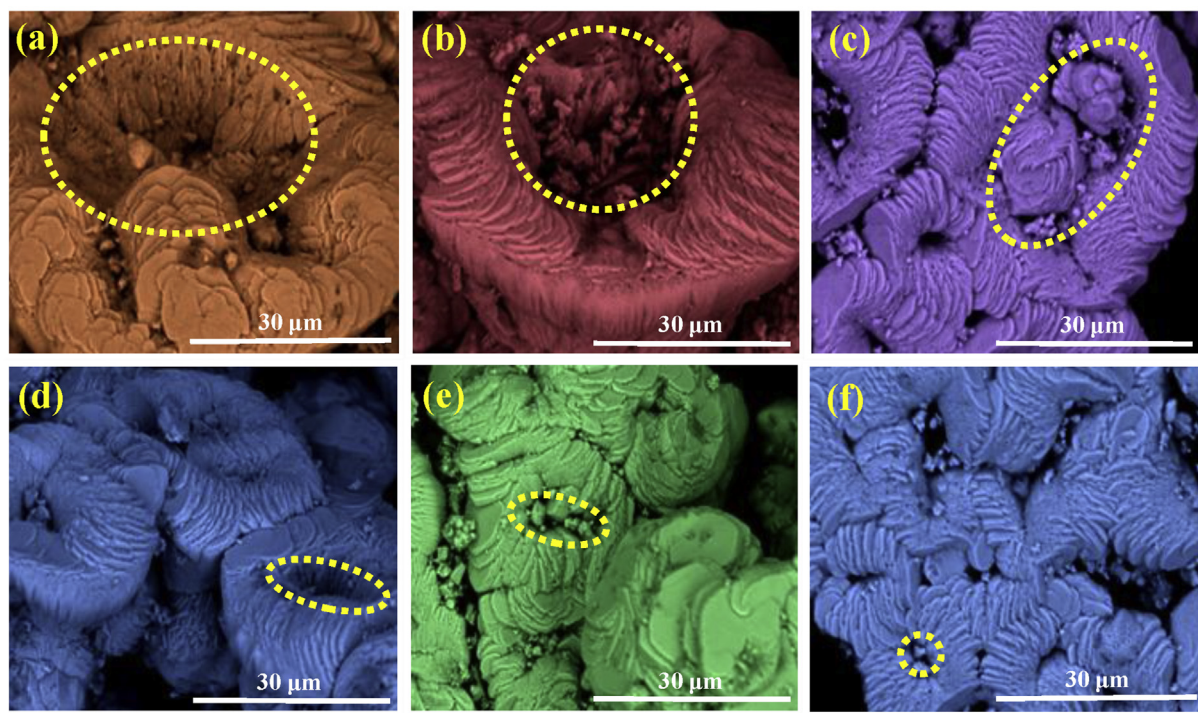

Fig. 5. SEM images of ZnO SS synthesized with various pH values (1, 3, 5, 7, 9 and 11) with *A.V.* gel concentration (35 mL) and ultrasonic irradiation time (6 h) were fixed.

Table 2
List of major phytochemicals extracted in *A.V.* gel confirmed from GCMS.

Name of the compound	Molecular weight	Molecular formula
Tetracontane	562	$C_{40}H_{82}$
Guanosine	283	$C_{10}H_{13}N_5O_5$
Ethanone, 1-Phenyl	120	C_8H_8O
Pentadecanoic acid	242	$C_{15}H_{30}O_2$

Self-sacrificial *A.V.* gel comprises several multifunctional organic compounds and active ingredients extracted using GCMS and the major components along with molecular was given in Table 2. The extract showed the major constituents such as Tetracontane (29.8%), Guanosine (19%), 1-phenyl ethanone (13%) and Pentadecanoic acid (6.8%) as reveled in the earlier report [27]. Among, the major Tetracontane has non-polar chain group and rest of the compounds contain both polar and non-polar heads. All these molecules become surfactant molecules and undergo self-assemble to form a micelle structure under certain conditions. The polar and non-polar heads of the micelle face exterior and interior respectively. Under ultrasound, polar heads of the organic molecules (micelle) would interact with the primary particles through physical amalgamation which can influence the bubble/solution interface, facilitates the typical crystallization and well aligned self-orientation to form the SS.

To know the effect of *A.V.* gel concentration on ZnO SS was studied in detail and shown in Fig. 6. When the *A.V.* gel concentration was 10 and 15 mL, oriented, self-assembled disc like structure were observed (Fig. 6(a and b)). However, the *A.V.* gel concentration was increased from 20 to 30 mL, organic molecules (micelle) present in *A.V.* gel would interact with the primary particles of ZnO to form a rough surfaced flower like architectures (Fig. 6(c–e)). When *A.V.* gel concentration was maintained to 35 mL, smooth surfaced well defined flower like SS was observed (Fig. 6(f)). SEM images of ZnO SS synthesized with different
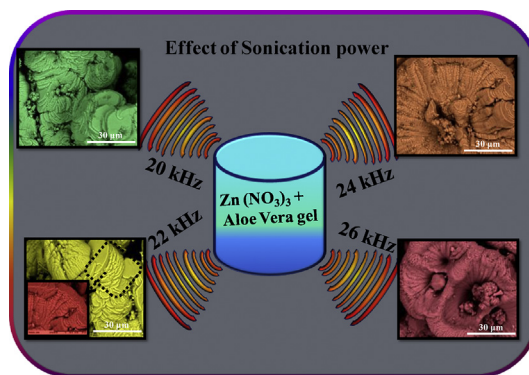

Fig. 7. SEM images of ZnO SS synthesized with different sonication power (20, 22, 24 and 26 kHz) with 3 h of ultrasonic irradiation time and pH value = 11.

sonication power (20, 22, 24 and 26 kHz) fabricated with 3 h of ultrasonic irradiation time and pH value = 11 was shown in Fig. 7. With increased sonication power leads well defined morphology was observed and it's evident that the sonication power can also influenced to engineer ZnO SS.

Fig. 8 shows the TEM, SAED patterns, HRTEM and AFM image of the ZnO SS synthesized with 3 h of the ultrasonic irradiation time, 35 mL of *A.V.* gel concentration and pH value = 11. It's evident from the TEM image, disc like shaped crystallite was observed (Fig. 8(a)). SAED pattern confirms that, all the diffraction rings were well indexed with hkl plane numbers (Inset Fig. 8(a)). The HRTEM image shows that the product was highly crystalline in nature with the interplanar spacing (d) values for (002) and (100) planes were found to be ~0.26 and 0.286 nm respectively (Fig. 8(b)). AFM images of ZnO SS in Z-axis and 3-D axis scan of 3.0 μm, 3.0 μm and 0.29 μm along X, Y and Z-axis respectively
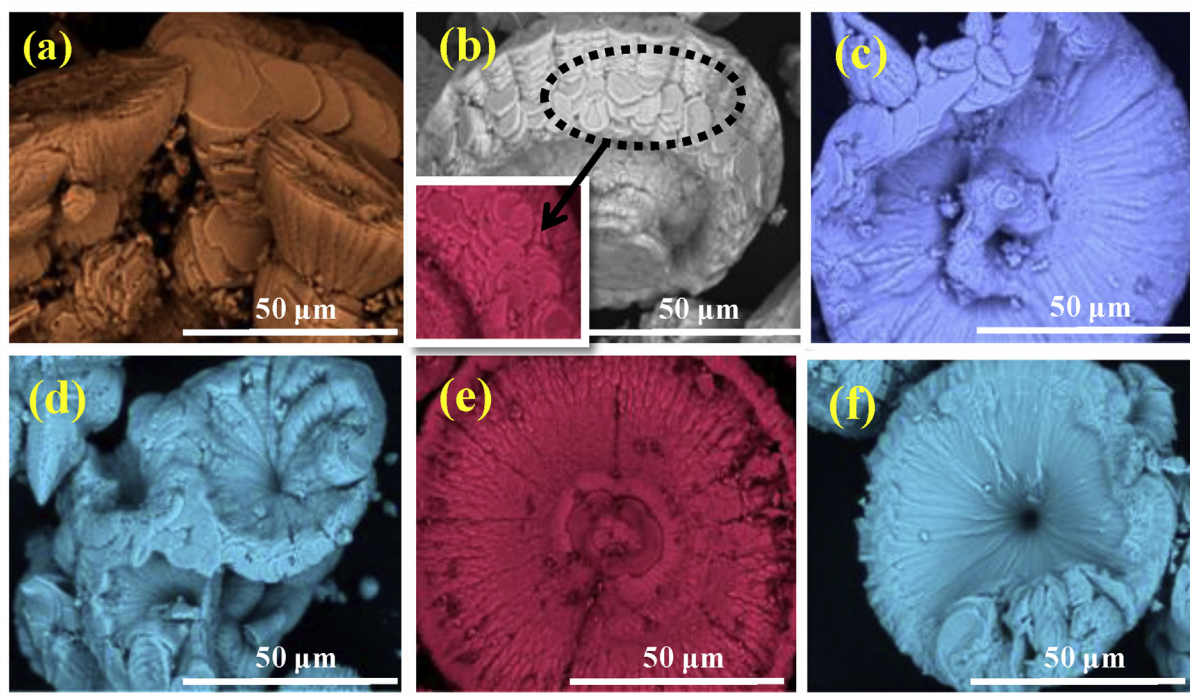

Fig. 6. SEM images of ZnO SS prepared with different concentration of *A.V.* gel (10, 15, 20, 25, 30 and 35 mL) with 3 h of ultrasonic irradiation time and pH value = 11.
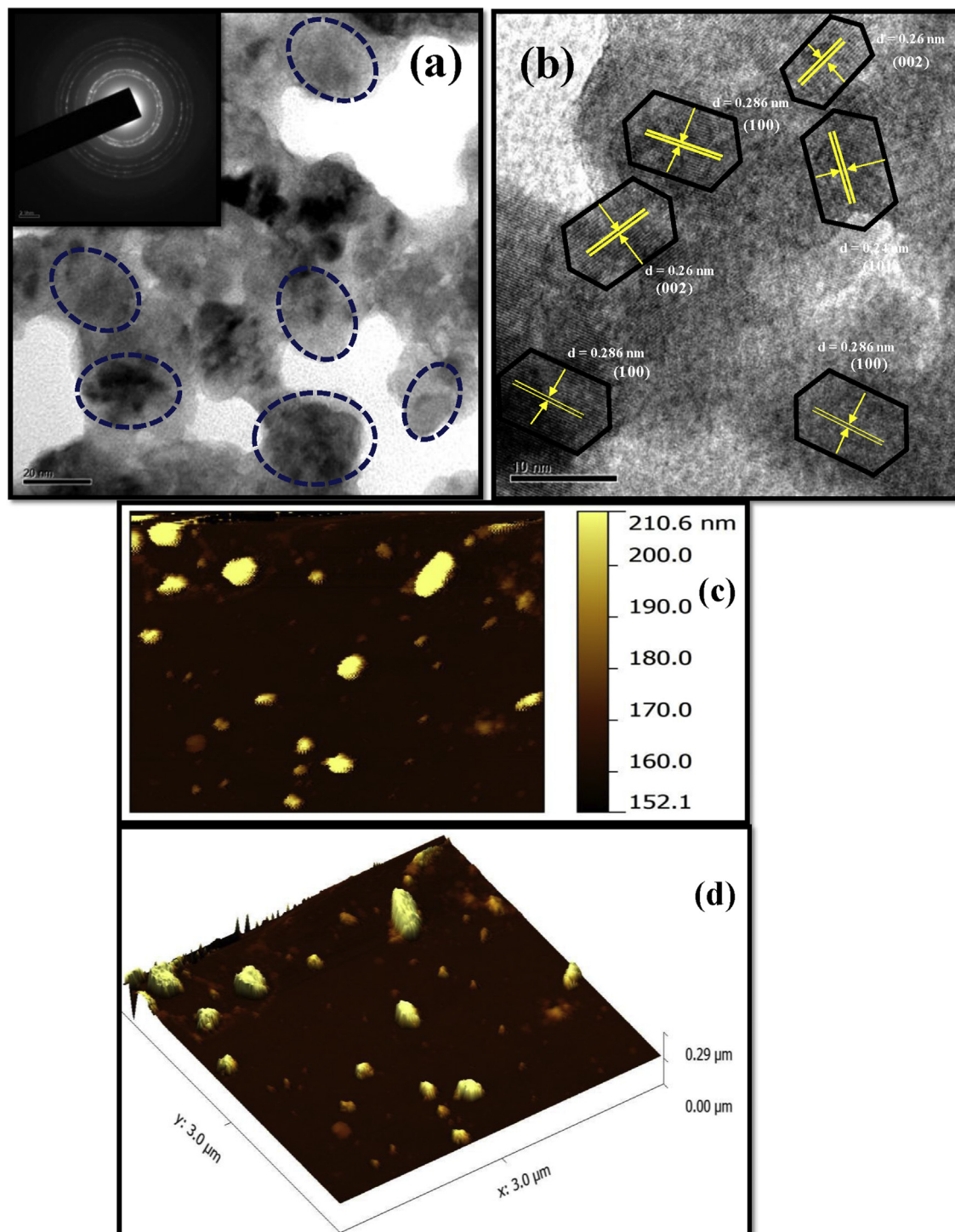
Fig. 8. (a) TEM (Inset SAED), (b) HRTEM, (c and d) AFM images of ZnO SS synthesized with 3 h of the ultrasonic irradiation time, 35 mL of *A.V.* gel concentration and pH value = 11.

(Fig. 8(c and d)). The image confirms the particular angle oriented ZnO SS from Z-axis.

Fig. 9(a) depict the PL excitation spectrum of ZnO SS at $\lambda_{emi} = 600$ nm. The spectrum exhibits a broad peak at ~390 nm may be attributed to exciton recombination or intrinsic defects. PL emission spectra of the ZnO SS fabricated by varying different experimental parameters at 390 nm excitation wavelengths were shown Fig. 9(b–d). The spectra exhibits a broad emission peak at ~508 nm and 600 nm. The de-convolution of the PL spectra was used for qualitative estimation of the defects present in the ZnO SS as per literature [28]. The de-convolution of the broad emission peak at 508 nm exhibits emission peak at ~414, 482, 524 and 603 nm attributed to Zinc interstitial (Zn_i), recombination between the Zn_i to the valence band level, Oxygen vacancy (V_o), and oxygen
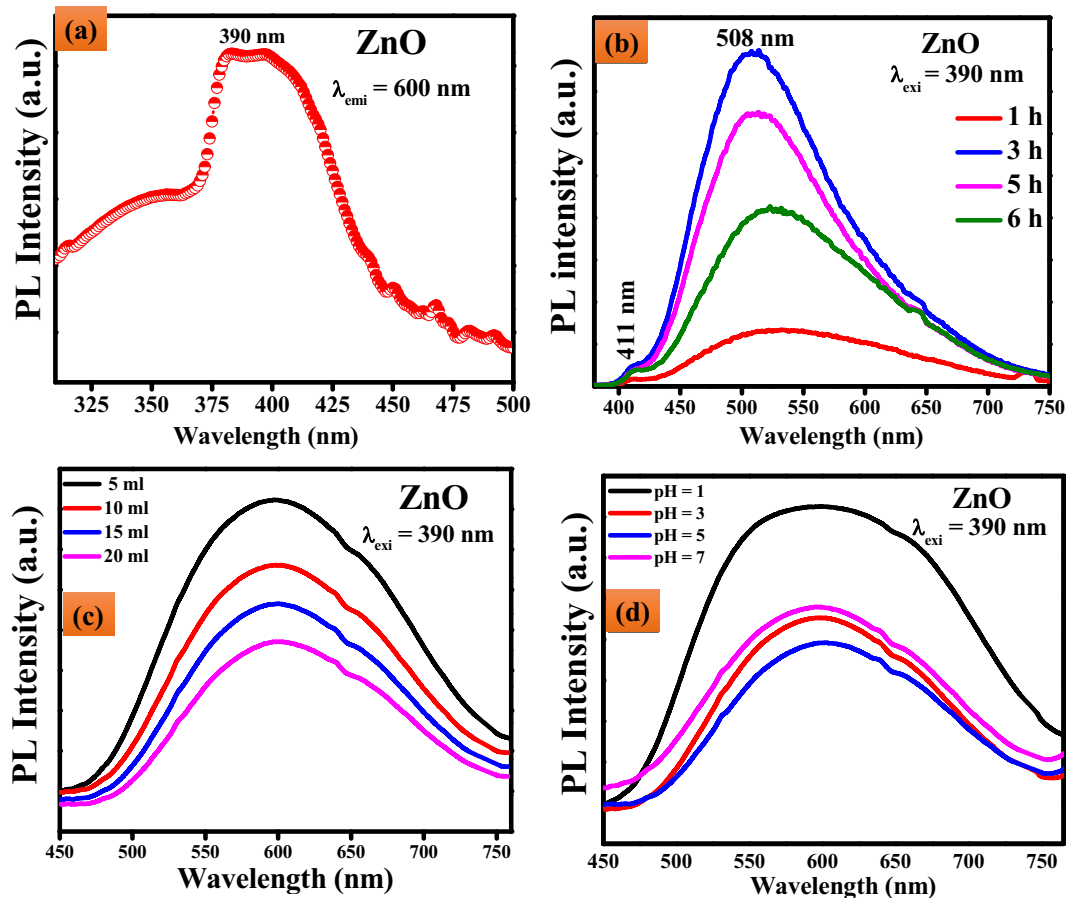
Fig. 9. (a) PL excitation spectrum, emission spectra of ZnO SS synthesized with different (b) sonication time, (c) concentration of *A.V.* gel and (d) pH values excited at 390 nm under RT.

interstitials (O$_i$) respectively (Fig. 10(a)). Similarly, the deconvolution of the PL spectra of ZnO SS synthesized with 5 mL of *A.V.* gel concentration exhibits defect related emission peaks at ~506, 530 nm (Blue green), 556, 600 nm (Yellow), 658 and 715 nm (Orange red) (Fig. 10(b)). A green emission peak at ~530 nm was usually due to recombination of trapped electrons in singly ionized oxygen vacancies (F$^+$ center or V$_0^+$) with photogenerated holes or zinc vacancies (V$_{zn}$). The studies revealed that the V$_{zn}$ can emit green luminescence, centered at a peak ~506 nm. The emission at 556 and 600 nm are attributed to doubly ionized oxygen vacancies (F^{2+} or V$_0^{2+}$) and oxygen interstitials (O$_i$) respectively [29]. The schematic energy level diagram of the emissions in the ZnO SS was shown in Fig. 10(e).

In general, the emission color of any phosphor can be represented by the (*x, y*) chromaticity co-ordinates in the Commission Internationale de L'Eclairage (CIE) 1931 diagram [30]. The CIE chromaticity diagram of 3D ZnO SS was shown in Fig. 10(c). The CIE co-ordinates were located in green, pale green and orange red region depends on different experimental parameters. The color correlated temperature (CCT) was one the important parameter to know the color appearance of the light emitted by a source, relating its color with respect to a reference light source when heated up to a specific temperature, in Kelvin (K) [37]. The CCT was calculated by transforming the (x, y) co-ordinates of the light source to (U$_0$, V$_0$) by using the relations by determining the temperature of the closest

point of the Planckian locus to the light source on the (*U′, V′*) uniform chromaticity diagram [31]:

$$U' = \frac{4x}{-2x + 12y + 3} \tag{3}$$

$$V' = \frac{9y}{-2x + 12y + 3} \tag{4}$$

Further, the quality of white light was checked in terms of CCT was given by McCamy empirical formula $CCT = -437n^3 + 3601n^2 - 6861n + 5514.31$ (theoretical) where $n = (x - x_c)/(y - y_c)$; the inverse slope line and chromaticity epicenter was at $x_c = 0.3320$ and $y_c = 0.1858$ [32]. The CCT diagram of prepared ZnO SS was shown in Fig. 10(d). The obtained values were well acceptable range and quite useful in commercial lighting application. The effect of sonication time, pH and *A.V.* gel concentration on the color purity of ZnO SS was also analyzed using the relation [33];

$$color\ purity = \frac{\sqrt{(x_s - x_i)^2 + (y_s - y_i)^2}}{\sqrt{(x_d - x_i)^2 + (y_d - y_i)^2}} \times 100\% \tag{5}$$
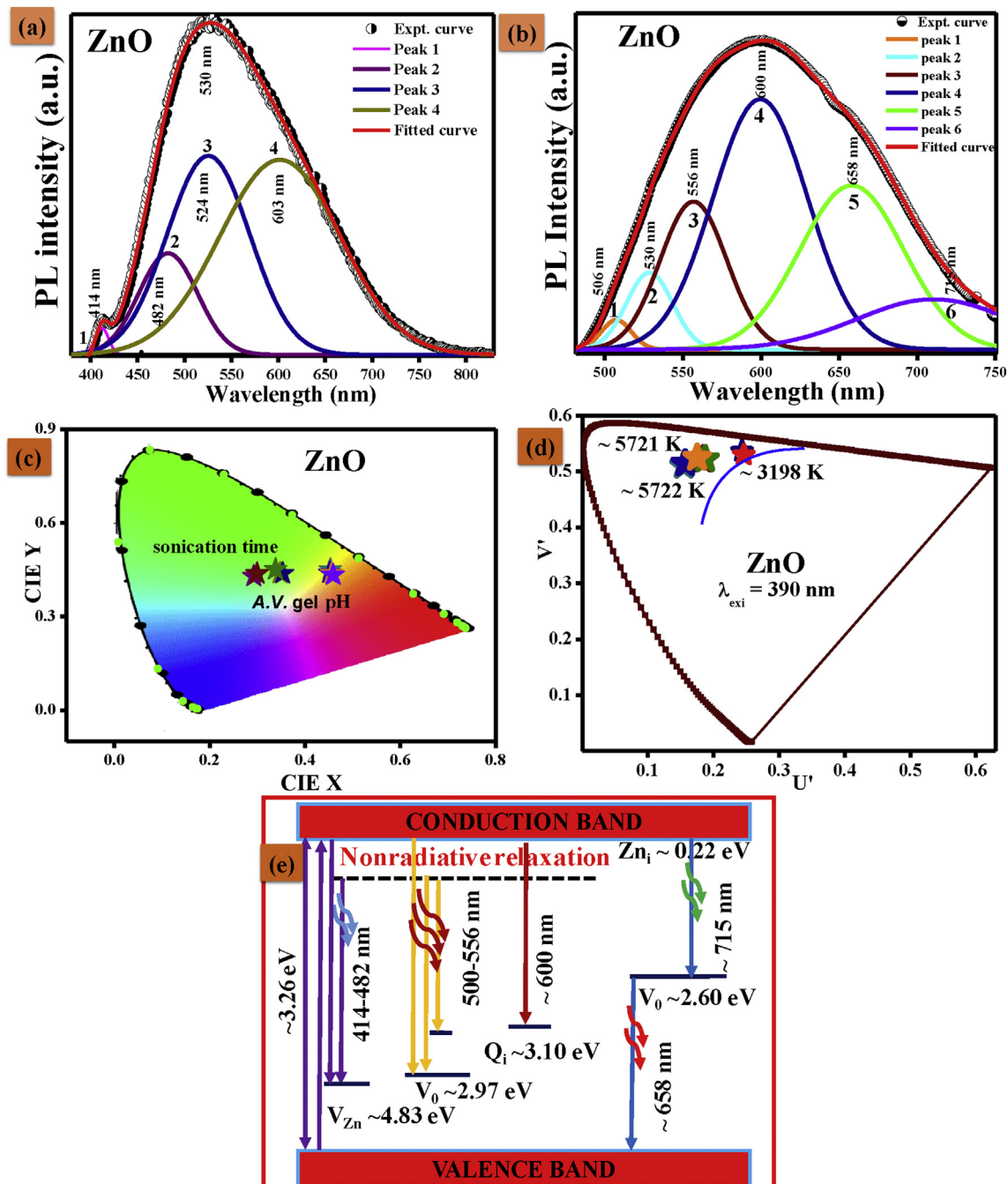
Fig. 10. Deconvoluted spectra of ZnO SS synthesized with (a) ultrasound irradiation time (3 h), (b) concentration of *A.V.* gel (5 mL), (c) CIE, (d) CCT diagram and (e) energy level diagram of ZnO SS.

where (x_s, y_s); the co-ordinates of a sample point, (x_d, y_d); the co-ordinates of the dominant wavelength and (x_i, y_i); the co-ordinates of the illuminant point. The estimated values of color purity of ZnO SS were found to be ~75–90%.

The Raman spectra of ZnO SS were measured in the range of 100–800 cm^{-1} was shown in Fig. 11(a). Based on the DFT calculations the second order phonon modes are divided into two regions: (i) the frequency range between 160 and 540 cm^{-1} is associated with the acoustic overtones, (ii) the frequency range of 540–820 cm^{-1} was attributed to the combinations of optical and acoustic phonon modes. In order to identify the separate phonon

modes, Raman spectrum was fitted using Lorentzian function and the de-convoluted spectrum was shown in Fig. 11(b). A characteristics sharp, strong, nonpolar optical phonon E$_{2H}$ mode located at ~441 cm^{-1} confirms the hexagonal wurtzite ZnO structure. The peak at ~333 and 410 cm^{-1} is ascribed to $E_{2H} - E_{2L}$ (multiphonon) and A$_{1T}$ modes respectively. The peaks at ~530 cm^{-1} is due to $2B_1$ (low) and 2 LA phonon modes. A phonon mode ~585 cm^{-1} is due to E$_1$ (LO) mode of ZnO. A weak intensity mode ~666 cm^{-1} can be ascribed to A$_{1g}$ modes of Zn$_2$ [34]. The Phonon lifetime measurements of ZnO SS were tabulated in Table 3.
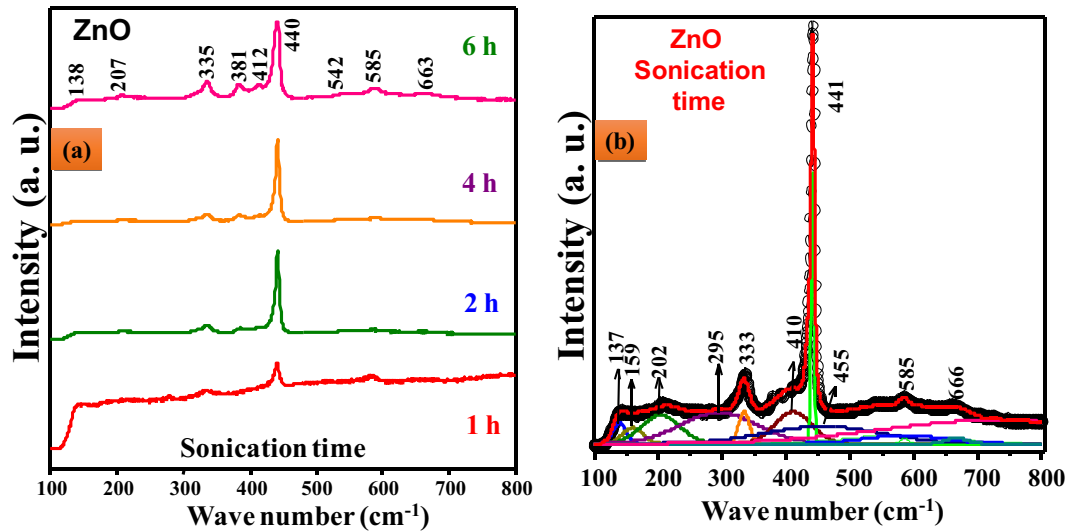
Fig. 11. (a) Raman spectra and (b) Deconvoluted Raman spectra of ZnO SS.

The DR spectra of 3D ZnO SS synthesized by varying ultrasound irradiation time, the pH of the solution and *A.V.* gel concentration were shown in Fig. 12(a, c and e). The spectra displays a strong band in the wavelength region ~450 nm was ascribed due to absorption of the host lattice. The Kubelka−Munk (K−M) theory was utilized to determine the energy band gap (E_g) synthesized ZnO SS from DR spectra. The Kubelka−Munk function $F(R_\infty)$ and photon energy ($h\nu$) was calculated by following equations [35]:

$$F(R_\infty) = \frac{(1 - R_\infty)^2}{2R_\infty} \tag{6}$$

$$h\nu = \frac{1240}{\lambda} \tag{7}$$

where R_∞; reflection coefficient of the sample, λ; the absorption wavelength. The intercept of the tangents to the plots of $[F(R_\infty)\, h\nu]^2$ versus photon energy $h\nu$ was shown in Fig. 12(b, d and f). The calculated E_g values were summarized in Table 1. The variation in E_g values were mainly attributed to degree of structural order and disorder in the matrix as well as change the distribution of energy levels within the band gap [36]. Furthermore, the degree of structural order−disorder of the matrix was mainly depends on the preparation methods as well as experimental conditions which can favor or slow up the formation of structural defects, which was also cause for the variation in the E_g.

In the present study, pathogenic microorganisms are usually selected, cataloged and standardized bacterial strains with significant clinical importance. These pathogenic microorganisms are responsible for numerous diseases, cases of hospital infection, colonization of medical devices, and have the ability to acquire resistance [37]. Furthermore, they are strains commonly used in studies of antibacterial activity of green synthesized SS. The MIC of an antibacterial agent for a given organism is the lowest concentration required to inhibit the growth of a bacterial growth in a standard test. The MBC is the minimal concentration of antibiotic that kills the inoculum and can be determined from broth dilution MIC tests by sub culturing to agar media without antibiotics. The MIC and MBC values of all the synthesized ZnO SS against bacteria are shown in Table 4. The ZnO SS showed significant inhibition against *S. aureus*, *B. subtilis*, *E. coli* and *P. aeruginosa*, with distinct differences in the susceptibility to ZnO SS in a dose-dependent manner. In relation to the MICs observed for the Gram-positive bacteria, there was a greater susceptibility to *B. subtilis* with 0.00025 μg/mL and to *S. aureus* with 0.025 μg/mL (Table 4). For the Gram-negatives, ZnO SS presented a MIC 2.5 μg/mL for *E. coli*. ZnO SS also presented a MIC of 0.000025 μg/mL for *P. aeruginosa* (the lowest observed in the Gram-negative bacteria) with ZnO SS prepared with plant extract (15 mL), it is also presenting a higher potency compared to all other conditions as shown in Table 4. In relation to MBC test, *P. aeruginosa* again showed a higher susceptibility to ZnO superstructures (0.00025 μg/mL) than to *E. coli* (2.5 μg/mL) and *B. subtilis* with 0.0025 μg/mL and to *S. aureus* with 0.25 μg/mL with SS and it showed identical results to the MIC test for both agents. However, superstructures prepared with different temperatures and pH was having higher than the above mentioned concentrations Table 4. The majority of investigations suggests that SS cause disruption of bacterial membranes probably by the creation of reactive oxygen species (ROS) such as super-oxide and hydroxyl radicals. As a nanoparticles reaches near the

Table 3
Phonon lifetime measurements of 3D ZnO SS.

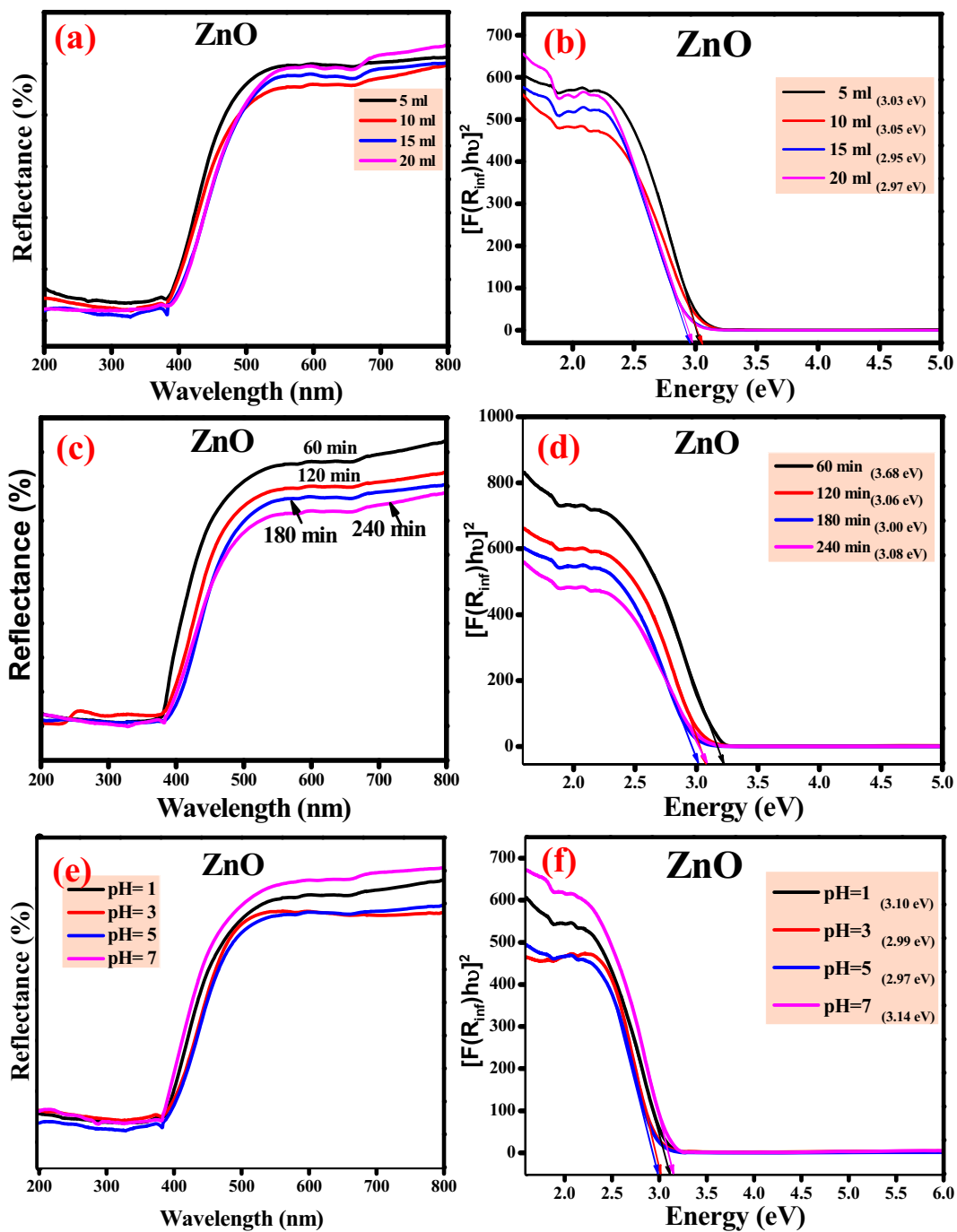| Reference (cm^{-1})	FWHM (Γ) (cm^{-1})	Phonon life time (τ) (μs)	Symmetry	Process
333	22.28	71.43	A1, (E$_2$, E$_1$)	E$_2^{high}$ − E$_2^{low}$
410	78.84	20.18	E$_1$	E$_1$ (TO)
441	5.42	293.64	E$_2$	E$_2^{high}$
585	26.16	60.83	E$_1$	E$_1$ (LO)
666	73.85	21.55	A$_1$	TA + LO

Fig. 12. DR spectra and their corresponding energy band gap plots of ZnO SS prepared by varying various experimental parameters.

Table 4
Percentage of inhibition by ZnO SS against *F. oxysporum* and *P. azadirachtae.*

Organism	ZnO SS	PC	NC	100	200	300	400
P. azadirachtae	pH (3.5)	0	100	34.183 ± 1.69004	37.360 ± 2.13429	49.440 ± 2.31234	68.430 ± 0.84451
	Sonication time (6 h)	0	100	37.360 ± 2.07719	44.480 ± 1.97228	57.853 ± 2.36204	62.500 ± 1.21791
	A.V. gel conc. (15 mL)	0	100	18.143 ± 2.53804	45.654 ± 2.59603	49.947 ± 5.51748	70.080 ± 8.21833
F. oxysporium	pH (5)	0	100	20.190 ± 1.48581	29.277 ± 1.62930	51.997 ± 0.72542	69.393 ± 0.87922
	pH (3.5)	0	100	28.040 ± 3.45670	35.033 ± 1.08657	53.910 ± 3.22348	64.990 ± 1.28187
	A.V. gel extract (15 mL)	0	100	19.750 ± 1.75077	34.863 ± 2.81134	48.250 ± 6.403117	66.667 ± 1.84598
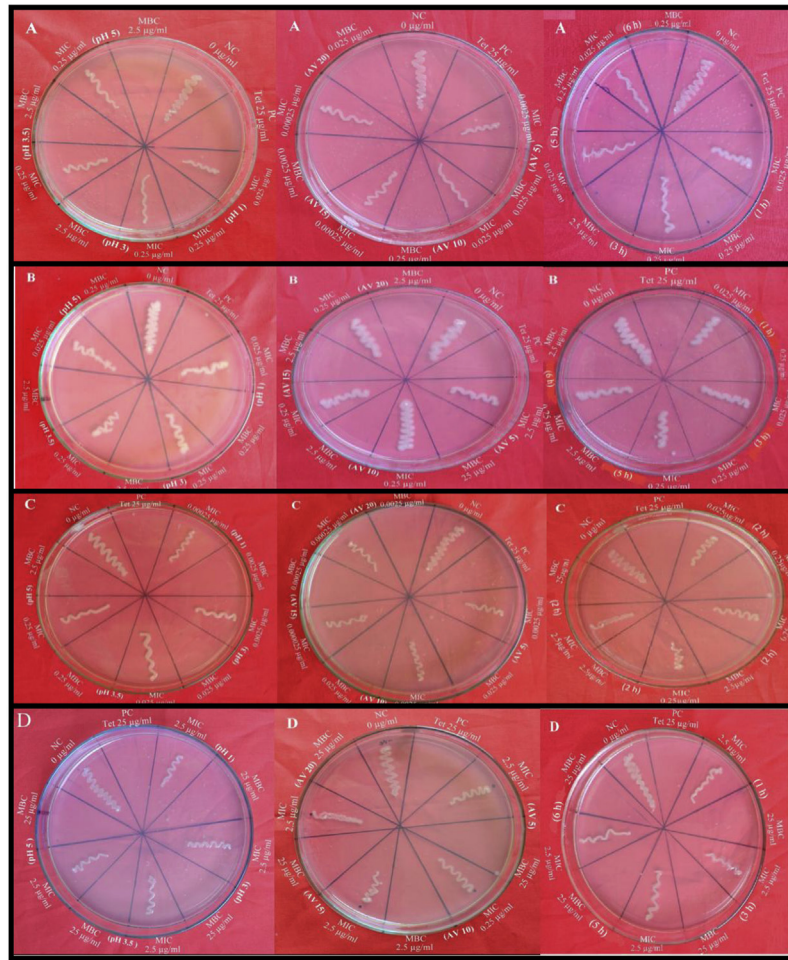
Note: Column 1= pH: 1, 3, 5 and 7; Column 2= *A.V.* gel: 5, 10, 15 and 20 ml; Column 3= sonication time: 1, 3, 5 and 6 h.

Fig. 13. Petri dishes streaked with (A) *Bacillus subtilis*, (B) *Staphylococcus aureus*, (C) *Pseudomonas aeruginosa*, (D) *Escherichia coli* showing MIC and MBC values of ZnO SS.

membrane, a potential called zeta potential is created. This is different for various types of superstructures. ZnO SS is known to have the positive zeta potential of their exterior. This depends on the nature of the surface of different microbes. Moreover, antimicrobial activity is also stated to be dependent on the concentration of the ZnO SS and impact of the type of reactant used (Fig. 13).

Fig. 14 shows the effect of ZnO SS on the growth of *P. azadirachtae* and *F. oxysporum* that were cultured on SDA containing different concentrations of ZnO SS (100, 200, 300 and 400 µg/mL) incubated at 25 °C for 7 days. Generally, the use of ZnO SS suspension was effective in inhibiting the fungal growth for both *P. azadirachtae* and *F. oxysporum* (Fig. 14). The average growth of *P. azadirachtae* and was inhibited by from 62% to 70% in terms of colony growth diameters after 7 days of incubation as the concentration of ZnO SS increased from 100 to 400 µg/mL with a near complete inhibition at 700 µg/mL (Table 4). For *F. oxysporum* (Fig. 14), the reduction rate of fungal growth varied from 64% to 69% as the concentration of ZnO SS increased from 100 to 400 µg/mL with a near complete inhibition at 700 µg/mL. A significant difference was found in different concentrations of

ZnO NP treatment ($P < 0.05$). These results indicate that ZnO SS at concentrations greater than 600 µg/mL can significantly inhibit the growth of *P. azadirachtae* and 700 µg/mL for *F. oxysporum*. This shows that ZnO SS were more effective against *P. azadirachtae* than that of *F. oxysporum*. Fig. 15 shows the effect of ZnO SS against (a) *F. oxysporum* and (b) *P. azadirachtae* with mean standard errors. The antimicrobial activities of the various inorganic SS such as S, Ag, CuO, MgO and ZnO were investigated distinctly or combined with biopolymer in previous studies [38]. Thus, it stimulated us to set up a new green nanoscale that leads to management of fungal phytopathogens using an antimicrobial SS to protect plant proficiently and eco-friendly. Such aims led us to focus on ZnO SS which are low-cost, stable and sensitive to pathogenic fungi [39]. Nano-biocide a product developed by mixing several bio-based chemicals was testified to eliminate fungus *Magnaporthe grisea*, the causal agent of rice blast disease [40]. Nano fungicides can be prepared in a simple, cost-effective manner are appropriate for formulating new categories of ZnO SS would be used as a novel eco-friendly antimicrobial for different fungal pathogenic organisms of the plant.
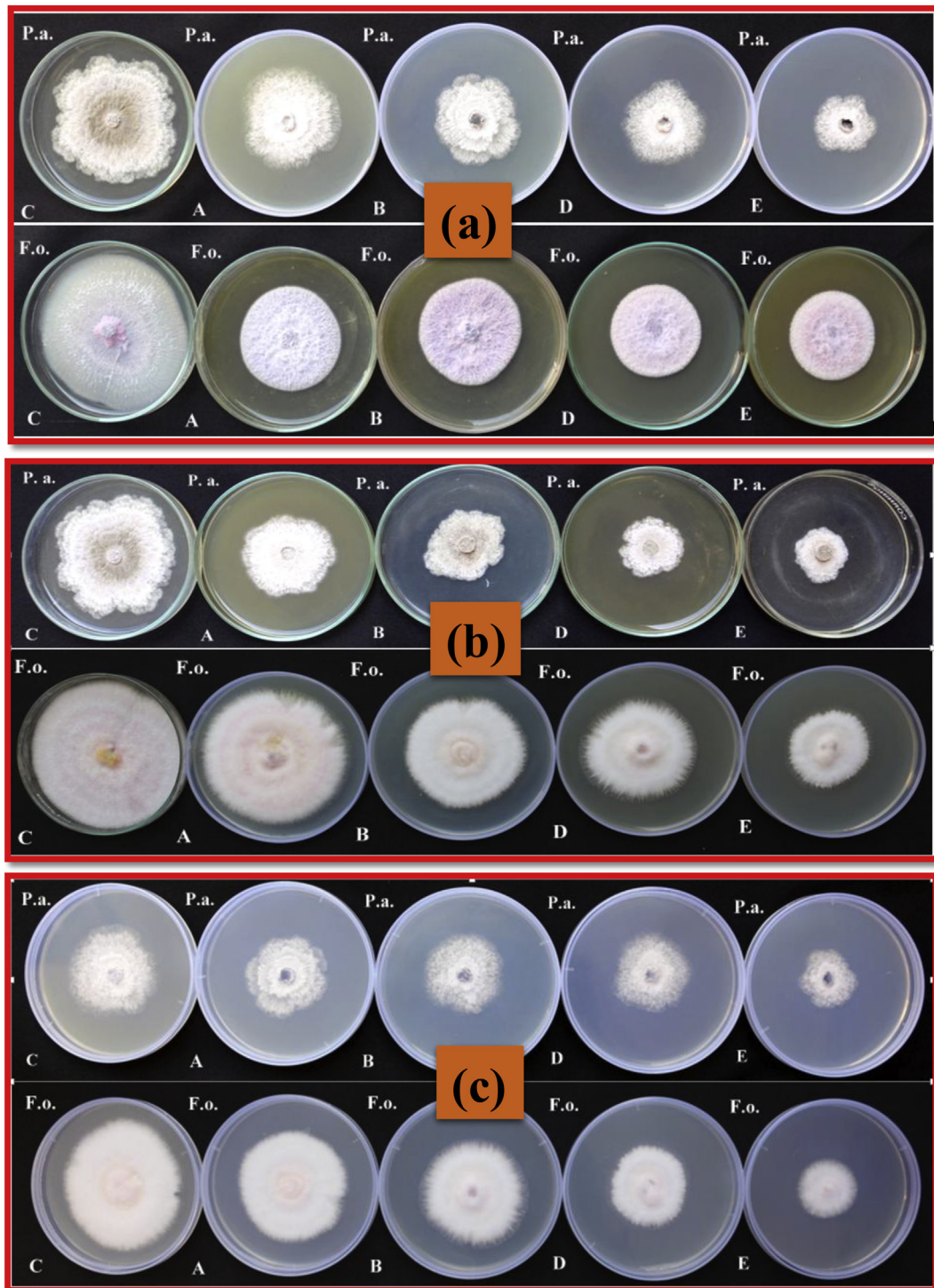
Fig. 14. The inhibitory effect of ZnO SS synthesized with (a) pH = 5, (b) sonication time (6 h) and (c) *A.V.* concentration (15 mL) on mycelial growth inhibition against *P. azadirachtae* and *F. oxysporum*. P.a.-*Phomopsis azadirachtae*, F.o-*Fusarium oxysporum*, C-Control, A-100 µg/mL, B-200 µg/mL, C-300 µg/mL, D-400 µg/mL, E-500 µg/mL.
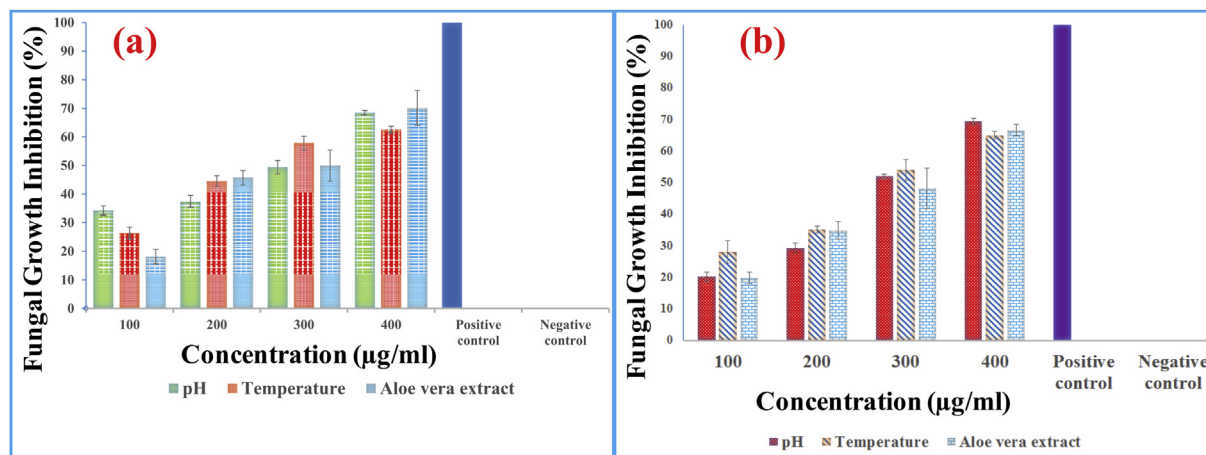
Fig. 15. Effect of ZnO SS against (a) *F. oxysporum* and (b) *P. azadirachtae*. The data are shown ± mean, standard error.

4. Conclusion

We have presented the synthesis of ZnO SS with explicit SS morphologies via a facile, bio-sacrificial *A.V.* gel assisted ultra-sonication method. Additionally, the shape, size and structures of the products can be successfully controlled by varying the reaction parameters such as ultrasound irradiation time, pH and *A.V.* gel concentration. The use of ultrasound and bio-template leads to large nucleation rates and hence to a large stabilized SS. The formation mechanism for the various morphologies was extensively studied. From PXRD spectra, the fabricated ZnO SS exhibits a hexagonal Wurtzite phase and is well indexed with JCPDS No 36-1451. The photometric properties of the samples could be easily tuned by varying the experimental parameters. Nano fungicides can be obtained in a simple, cost-effective manner and are suitable for articulating new categories of nano biotic constituents, which would be used as an innovative eco friendly, antimicrobial for diverse mycopathogenic organisms of plants.

Acknowledgments

References

[1] P. Jiang, J.J. Zhou, H.F. Fang, C.Y. Wang, Z.L. Wang, S.S. Xie, Hierarchical shelled ZnO structures made of bunched nanowire arrays, Adv. Funct. Mater 17 (2007) 1303–1310.

[2] J.Y. Lao, I.G. Wen, Z.F. Ren, Hierarchical ZnO nanostructures, Nano Lett. 2 (2002) 1287–1291.

[3] Huanhuan Wang, Jianyi Lin, Ze Xiang Shen, Polyaniline (PANi) based electrode materials for energy storage and conversion, J. Sci. Adv. Mater. Dev. 1 (2016) 225–255.

[4] X.F. Zhou, D.Y. Zhang, Y. Zhu, Y.Q. Shen, X.F. Guo, W.P. Ding, Mechanistic investigations of PEG-directed assembly of one-dimensional ZnO nanostructures, J. Phys. Chem. B 110 (2006) 25734–25739.

[5] T.P. Chou, Q.F. Zhang, G.E. Fryxell, G.Z. Cao, Hierarchically structured ZnO film for dye-sensitized solar cells with enhanced energy conversion efficiency, Adv. Mater. 19 (2007) 2588–2592.

[6] Y.Q. Yang, G.H. Du, X. Xin, B.S. Xu, Hierarchical ZnO microrods: synthesis, structure, optical and photocatalytic properties, Appl. Phys. A 104 (2011) 1229–1235.

[7] Krishnendu Chatterjee, Sreerupa Sarkar, K. Jagajjanani Rao, Santanu Paria, Core/shell nanoparticles in biomedical applications, Adv. Colloid Interface Sci. 209 (2014) 8–39.

[8] F. Domenici, C. Fasolato, E. Mazzi, L. De Angelis, F. Brasili, F. Mura, P. Postorino, F. Bordi, Engineering microscale two-dimensional gold nanoparticle cluster arrays for advanced Raman sensing: an AFM study, Colloids Surf. A: Physicochem. Eng. Asp. 498 (2016) 168–175.

[9] H. Nagabhushana, R.B. Basavaraj, B. Daruka Prasad, S.C. Sharma, H.B. Prem kumar, Udayabhanu, G.R. Vijayakumar, Facile EGCG assisted green synthesis of raspberry shaped CdO nanoparticles, J. Alloys Compd. 669 (2016) 232–239.

[10] G.P. Darshan, H.B. Premkumar, H. Nagabhushana, S.C. Sharma, B. Daruka Prasad, S.C. Prashantha, R.B. Basavaraj, Superstructures of doped yttrium aluminates for luminescent and advanced forensic investigations, J. Alloys Compd. 686 (2016) 577–587.

[11] Ananda J. Jadhav, Dipak V. Pinjari, Aniruddha B. Pandit, Surfactant assisted sonochemical synthesis of hollow structured zinc phosphate nanoparticles and their application as nanocarrier, Chem. Eng. J. 297 (2016) 116–120.

[12] H.J. Amith Yadav, B. Eraiah, H. Nagabhushana, G.P. Darshan, B. Daruka Prasad, S.C. Sharma, H.B. Premkumar, K.S. Anantharaju, G.R. Vijayakumar, Facile ultrasound route to prepare micro/nano superstructures for multifunctional applications, ACS Sustainable Chem. Eng. 5 (2017) 2061–2074.

[13] C. Suresh, H. Nagabhushana, G.P. Darshan, R.B. Basavaraj, B. Daruka Prasad, S.C. Sharma, M.K. Sateesh, J.P. Shabaaz Begum, Lanthanum oxyfluoride nanostructures prepared by modified sonochemical method and their use in the fields of optoelectronics and biotechnology, Arabian J Chem (2017), https://doi.org/10.1016/j.arabjc.2017.03.006.

[14] C. Suresh, H. Nagabhushana, R.B. Basavaraj, B. Daruka Prasad, Green light emitting nanostructures of Tb^{3+} doped LaOF prepared via ultrasound route applicable in display devices, AIP Conf. Proc. 1832 (2017) 050143.

[15] Zhengwei Chen, Xu Wang, Fabi Zhang, Shinji Noda, Katsuhiko Saito, Tooru Tanaka, Mitsuhiro Nishio, Qixin Guo, Temperature dependence of luminescence spectra in europium doped Ga$_2$O$_3$ film, J. Lumin 177 (2016) 48–53.

[16] Geun-Hyoung Lee, Morphology and luminescence properties of ZnO micro/nanostructures synthesized via thermal evaporation of Zn–Mg mixtures, Ceram. Int. 41 (2015) 8475–8480.

[17] Saikumar Inguva, Ciarán Gray, Enda McGlynn, Jean-Paul Mosnier, Origin of the 3.331 eV emission in ZnO nanorods: comparison of vapour phase transport and pulsed laser deposition grown nanorods, J. Lumin 175 (2016) 117–121.

[18] W. Chebil, M.A. Boukadhaba, A. Fouzri, Epitaxial growth of ZnO on quartz substrate by sol-gel spin-coating method, Superlattices Microstruct. 95 (2016) 48–55.

[19] Adem Sreedhar, Jin Hyuk Kwon, Jonghoon Yi, Jong Su Kim, Jin Seog Gwag, Enhanced photoluminescence properties of Cu-doped ZnO thin films deposited by simultaneous RF and DC magnetron sputtering, Mater. Sci. Semicond. Process 49 (2016) 8–14.

[20] P.S. Shewale, Y.S. Yu, The effects of pulse repetition rate on the structural, surface morphological and UV photodetection properties of pulsed laser deposited Mg-doped ZnO nanorods, Ceram. Int. 42 (6) (2016) 7125–7134.

[21] Xiurong Qu, Shuchen Lü, Jingju Wang, Zhongqiu Li, Huijie Xue, Preparation and optical property of porous ZnO nanobelts, Mater. Sci. Semicond. Process 15 (2012) 244–250.

[22] Zhigang Zang, Mengqing Wen, Weiwei Chen, Yangfu Zeng, Zhiqiang Zu, Xiaofeng Zeng, Xiaosheng Tang, Strong yellow emission of ZnO hollow nanospheres fabricated using polystyrene spheres as templates, Mater. Des. 84 (2015) 418–421.

[23] M. Chandrasekhar, H. Nagabhushana, S.C. Sharma, K.H. Sudheerkumar, N. Dhananjaya, D.V. Sunitha, C. Shivakumara, B.M. Nagabhushana, Particle size, morphology and color tunable ZnO: Eu^{3+} nanophosphors via plant latex mediated green combustion synthesis, J. Alloys Compd. 25 (2014) 417–424.

[24] A. Jagannatha Reddy, M.K. Kokila, H. Nagabhushana, R.P.S. Chakradhar, C. Shivakumara, J.L. Rao, B.M. Nagabhushana, Structural, optical and EPR studies on ZnO: Cu nanopowders prepared via low temperature solution combustion synthesis, J. Alloys Compd. 509 (2011) 5349–5355.

[25] Praloy Mondal, Debajyoti Das, Transparent and conducting intrinsic ZnO thin films prepared at high growth-rate with c-axis orientation and pyramidal surface texture, Appl. Surf. Sci. 286 (2013) 397–404.

[26] M. Venkataravanappa, H. Nagabhushana, G.P. Darshan, B. Daruka Prasad, G.R. Vijayakumar, H.B. Premkumar, Udayabhanu, Novel EGCG assisted ultrasound synthesis of self-assembled Ca_2SiO_4: Eu^{3+} hierarchical superstructures: photometric characteristics and LED applications, Ultrason. Sonochem 33 (2016) 226–239.

[27] K. Alia, S. Dwivedi, A. Azam, Q. Saquib, M.S. Al-Said, A.A. Alkhedhairy, J. Musarrat, Aloe vera extract functionalized zinc oxide nanoparticles as nanoantibiotics against multi-drug resistant clinical bacterial isolates, Accepted manuscript, J. Colloid Interface Sci..

[28] A. Sahai, N. Goswami, Probing the dominance of interstitial oxygen defects in ZnO nanoparticles through structural and optical characterizations, Ceram. Int. 40 (2014) 14569–14578.

[29] Mehrdad Najafi, Hamid Haratizadeh, The effects of Al doping and post-annealing via intrinsic defects on photoluminescence properties of ZnO: Eu nanosheets, Mater. Sci. Semicond. Process 31 (2015) 76–83.

[30] Publication CIE no 17.4, International Lighting Vocabulary, Central Bureau of the Commission Internationale de L'Eclairage, Vienna, Austria, 1987.

[31] M. Dhanalakshmi, H. Nagabhushana, G.P. Darshan, R.B. Basavaraj, B. Daruka Prasad, Sonochemically assisted hollow/solid $BaTiO_3$:Dy^{3+} microspheres and their applications in effective detection of latent fingerprints and lips prints, J. Sci. Adv. Mater. Devices 2 (2017) 22–33.

[32] K.N. Venkatachalaiah, H. Nagabhushana, G.P. Darshan, R.B. Basavaraj, B. Daruka Prasad, Novel and highly efficient red luminescent sensor based SiO_2@Y_2O_3:Eu^{3+}, M^+ (M^+= Li, Na, K) composite core–shell fluorescent markers for latent fingerprint recognition, security ink and solid state lightning applications, Sens. Actuators B 251 (2017) 310–325.

[33] K.N. Venkatachalaiah, H. Nagabhushana, G.P. Darshan, R.B. Basavaraj, B. Daruka Prasad, S.C. Sharma, Blue light emitting Y_2O_3:Tm^3 $^+$ nanophosphors with tunable morphology obtained by bio-surfactant assisted sonochemical route, Spectrochim. Acta Part A Mol. Biomole. Spect. 184 (2017) 89–100.

[34] Animesh K. Ojha, Manish Srivastava, Sumeet Kumar, Rasha Hassanein, Jay Singh, Manish K. Singh, Arnulf Materny, Influence of crystal size on the electron–phonon coupling in ZnO nanocrystals investigated by Raman spectroscopy, Vib. Spec. 72 (2014) 90–96.

[35] G.P. Darshan, H.B. Premkumar, H. Nagabhushana, S.C. Sharma, S.C. Prashantha, H.P. Nagaswarup, B. Daruka Prasad, Blue light emitting ceramic nano-pigments of Tm^{3+} doped $YAlO_3$: applications in latent finger print, anti-counterfeiting and porcelain stoneware, Dyes Pig 131 (2016) 268–281.

[36] G.P. Darshan, H.B. Premkumar, H. Nagabhushana, S.C. Sharma, S.C. Prashanth, B. Daruka Prasad, Effective fingerprint recognition technique using doped yttrium aluminate nano phosphor material, J. Colloid Interface Sci. 464 (2016) 206–218.

[37] P.V.M. Toledo, L.N. Arend, M. Pilonetto, J.C. Costa Oliveira, K.R. Luhm, Surveillance programme for multidrug-resistant bacteria in healthcare-associated infections: an urban perspective in South Brazil, J. Hosp. Infect. 80 (2012) 351–353.

[38] M. Rai, A. Ingle, Role of nano technology in agriculture with special reference to management of insect pests, Appl. Microbiol. Biotechnol. 94 (2012) 287–293.

[39] K.A. Abd-Elsalam, M.A. Alghuthaymi, Nanobio-fungicides: are they the next-generation of fungicides, J. Nanotech. Mater. Sci. 2 (2015) 1–3.

[40] R. Gogoi, P. Dureja, P.K. Singh, Nano formulations a safer and effective option for agrochemicals, Indian Farming 59 (2009) 7–12.